One-Step Pyrolysis Construction of Bimetallic Atom-Cluster Sites for Boosting Bifunctional Catalytic Activity in Zn-Air Batteries

Youpeng Wang, Naman Katyal, Yang Tang, Hua Li, Kihyun Shin, Wenqian Liu, Ruilin He, Maowen Xu, Graeme Henkelman,* and Shu-Juan Bao*

Due to their unique advantages, single atoms and clusters of transition metals are expected to achieve a breakthrough in catalytic activity, but large-scale production of active materials remains a challenge. In this work, a simple solvent-free one-step annealing method is developed and applied to construct diatomic and cluster active sites in activated carbon by utilizing the strong anchoring ability of phenanthroline to metal ions, which can be scaled for mass productions. Benefiting from the synergy between the different metals, the obtained sub-nano-bimetallic atom-cluster catalysts (FeNi$_{AC}$-NC) exhibit high oxygen reduction reactions (ORR) activity ($E_{1/2}$ = 0.936 V vs. RHE) and a small ORR/oxygen evolution reaction (OER) potential gap of only 0.594 V. An in-house pouch Zn-air battery is assembled using an FeNi$_{AC}$-NC catalyst, which demonstrates a stability of 1000 h, outperforming previous reports. The existence of clusters and their effects on catalytic activity is analyzed by density functional theory calculations to reveal the chemistry of nano-bimetallic atom-cluster catalysts.

1. Introduction

Ongoing environmental problems and increasing demands on energy supplies require rapid development of cleaner energy

Y. Wang, Y. Tang, W. Liu, R. He, M. Xu, S.-J. Bao
School of Materials and Energy
Southwest University
Chongqing 400715, P. R. China
E-mail: baoshj@swu.edu.cn
N. Katyal, K. Shin, G. Henkelman
Department of Chemistry
The University of Texas at Austin
Austin, TX 78712, USA
E-mail: henkelman@utexas.edu
H. Li
School of Materials and Energy
Electron Microscopy Centre
Lanzhou University
Lanzhou 730000, P. R. China
K. Shin
Department of Materials Science and Engineering
Hanbat National University
Daejeon 34158, Republic of Korea

conversion and storage devices. Among these emerging devices, zinc-air batteries have attracted attention for their high energy density, high safety, and low cost.[1,2] However, limited by the slow kinetics of the oxygen reduction reactions (ORR) and oxygen evolution reaction (OER) of the air electrode, zinc-air batteries suffer from inadequate catalytic activity and low round-trip efficiency.[3,4] Therefore, the design of a highly active ORR/OER bifunctional catalyst is critical.

Noble metal-based (Pt, Ru, Ir, etc.) materials, which have been developed and commercialized due to their high electrocatalytic performance, are considered as benchmarks for advanced catalysts, but their high price hinders widespread application.[5–8] For this reason, researchers have targeted non-precious metal catalysts. Especially, with the exploration of sub-nanometer catalysts, non-precious metal catalysts have sprung up and demonstrated strong potential due to their high atomic utilization as well as their well-defined active sites and tunable electronic environment.[9–12] Among them, carbon-supported single-atom catalysts, such as FeN$_4$ have been reported to exhibit excellent catalytic activity.[13–16] Although FeN$_4$ single atom catalysts can show outstanding catalytic activity, they have some disadvantages, including: 1) the single catalytic site of FeN$_4$ has not been shown to overcome the limitation of speeding up multi-step and multi-intermediate reactions,[17] many researchers have found that a high adsorption energy of single-atom FeN$_4$ catalysts toward intermediates *OH during ORR prevents the reaction from proceeding more rapidly;[18,19] and ② FeN$_4$ has a single active site, which cannot meet the practical application requirements of secondary zinc-air batteries.[20–22] During the charging and discharging process, the air electrode not only has to go through the ORR process, but also the OER process, and the sluggish ORR and OER of air electrode are the primary bottlenecks restricting the development of high-performance rechargeable ZABs. How to construct highly active bifunctional electrocatalysts that can afford electrocatalytic activity for both ORR and OER is important for reducing the large charge-discharge voltage gap and poor energy efficiency.

To this end, various strategies have been developed for tuning the electronic structure of the active sites of FeN$_4$-based catalyst

**ADVANCED
SCIENCE NEWS**

www.advancedsciencenews.com

**NANO · MICRO
small**

www.small-journal.com

to enhance its intrinsic catalytic activity and stability further. Introducing a second metal and exploiting the synergistic effect between different metal atoms to adjust the adsorption energy of Fe centers toward mutistep reaction intermediates and reduce potential barriers is a common strategy, which is confirmed by the excellent catalytical activity of N-doped carbon-supported FeCo, FeNi, and FeMn diatomic catalysts. Increasing the number of active sites by enhancing the metal content can also increase the catalytic activity of the catalyst. When the metal loading reaches a certain level, the appearance of clusters can bring unique effects. It was recently shown that for Fe–N–C catalysts, the interaction between single Fe atoms and Fe-clusters can induce charge redistribution in the single Fe atom centers through Fe-clusters, which attenuates the adsorption of *OH intermediates and improves the catalytic activity of Fe–N–C catalysts[23,24]; additionally the pinning effect through Fe-clusters suppresses the thermal vibrations of the satellite Fe–N sites, which reduces the tendency of metal detachment and improves the stability.[25] Therefore, synergizing bimetallic alloy clusters with bimetallic atomic structures can also bring the activity and stability of non-noble metals-based catalysts to a higher level, but few related studies have been reported.

Precise synthesis of such sub-nanocatalysts is a prerequisite for theoretical research and a guarantee for practical applications. However, it is still a great challenge because the preparation requires different metal ion coordination with N at the same sites, and the metal atoms are protected from agglomeration during high-temperature annealing,[26,27] and this method should be simple and facile for large-scale preparation. The primary synthetic methods for the preparation of single-cluster catalysts can be summarized as bottom-up and top-down approaches[28]: Bottom-up approaches generally use ligands to capture metal ions, which are then reduced and confined in a certain space to form bimetallic sub-nanocatalysts. Among them, wet chemical methods are most common, whereas atomic layer deposition (ALD) is an emerging powerful technique for building atomic-scale catalysts.[29,30] The top-down approach is primarily achieved by high-temperature pyrolysis of metal-organic complexes.[31–33] Although ALD enables precise regulation at the atomic scale, it cannot be achieved without the support of advanced equipment. Most wet chemical and top-down methods require solvents, which inevitably involve solid-liquid separation, increasing the workload for large-scale production.[34,35] Therefore, not only the potential catalytic activity mechanism of such bimetallic sub-nanocatalysts needs to be investigated in-depth, but also simple and effective preparation methods.

Here, a bimetallic catalyst was synthesized where ferrocene and nickelocene were used as metal sources, and phenanthroline was used as the nitrogen source and metal-anchoring agent. Due to the strong coordination ability of the vaporized ferrocene and nickelocene, the liquefied phenanthroline can coordinate ferrocene/nickelocene and carry them freely into the pores of activated carbon. After a simple one-step pyrolysis process, the FeNi were accommodated into commercialized activated carbon by forming metal and nitrogen sites. More importantly, the coordination capacity of phenanthroline is limited. Hence, by adjusting the feed ratio of phenanthroline to that of ferrocene/nickelocene, the density of FeNi sites can be controlled for bimetallic atoms and clusters. Compared to other methods, our proposed one-step

dry method is very simple and can be developed for large-scale production. In particular, our prepared FeNi atom-cluster catalyst (FeNi$_{AC}$-NC) exhibits an extremely high ORR ($E_{1/2}$ = 0.936 V vs. RHE) and OER performance ($E_{@50\ mA}$ = 1.664 V vs. RHE), exhibiting a remarkable discharge performance and stability of an in-house pouch Zn-air battery (stable cycling for 1000 h), which is a better result than most reports. A series of density functional theory (DFT) calculations were also carried out, which confirms the bonding mode of Fe and Ni with N and the coexistence of FeNi double atoms and clusters in our prepared materials. DFT calculations of bimetallic FeNi catalyst (the content ratio of Fe:Ni = 1:1) demonstrate the superior ORR and OER activity compared to single atom Fe and Ni catalyst, which can be explained by a change in the rate-determining step due to interactions between Fe and Ni.
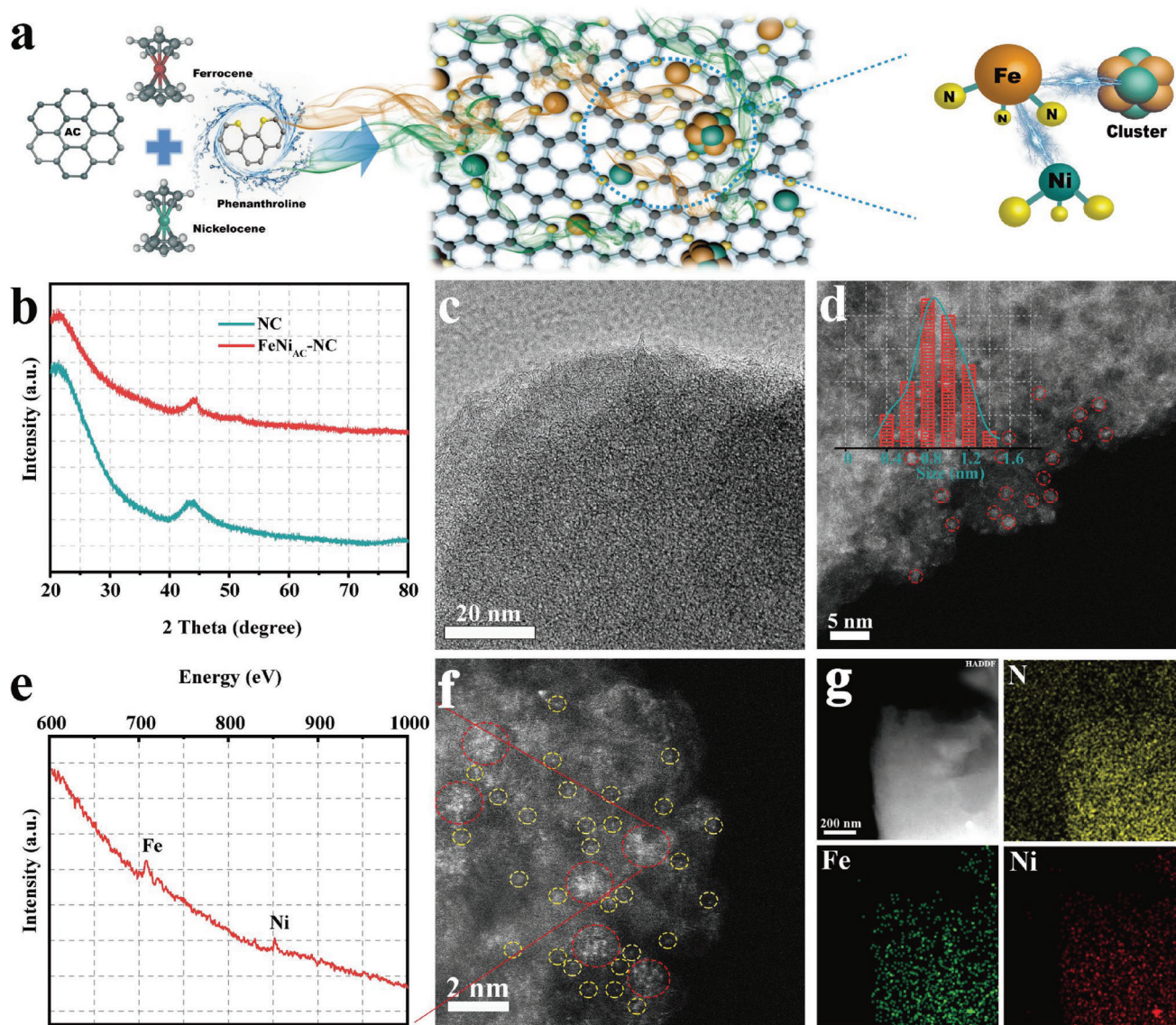
2. Results and Discussion

2.1. Morphology Characterization and Active Site Structure Analysis

FeNi$_{AC}$-NC was synthesized by one-step pyrolysis of phenanthroline, activated carbon, ferrocene, and nickelocene. Specifically, the melting temperature of phenanthroline is 117 °C, and the sandwich compound like ferrocene and nickelocene are easy to sublimate above 100 °C. As shown in **Figure 1**a, at a temperature of 120 °C, the liquefied phenanthroline can freely adsorb on the carbon surface and enter its pores by carrying the vaporized ferrocene and nickelocene because of its strong coordination ability. Due to the limited anchoring capacity of the phenanthroline and the pore site resistance of the activated carbon, the limited metals are immobilized on the activated carbon to form single-atom and cluster catalysts during further annealing.

Notably, in order to study the form of Fe and Ni in nitrogen-doped carbon, metal-free samples with nitrogen-doped carbon (NC) were also prepared under the same conditions. Compared to NC, the XRD of the FeNi$_{AC}$-NC exhibited very weak metal peaks, suggesting small metal clusters or atoms immobilized on the carbon. TEM and magnified HAADF-STEM were conducted to elucidate the form of the remaining Fe and Ni on carbon. No metal particles can be seen on the surface of AC in the TEM image (Figure 1c), while the magnified HAADF-STEM revealed homogeneously distributed small bright dots, attributed to heavier Fe, and Ni over light N, and C atoms. The regions circled in red contain metal clusters of Fe/Ni (Figure 1d) with sizes distributed in the 0.8–1.2 nm range. A further magnified HADFF-STEM image (Figure 1f) and its corresponding EEL spectrum suggest that the clusters are homogeneously composed of Fe and Ni. In addition to the clusters, there are many uniformly distributed smaller bright spots circled in yellow, which should be single atoms of Fe and Ni, indicating that the sample is composed of bimetallic clusters and single atoms of the two metals. These single atoms are close to the clusters, which facilitates electron transport between the cluster and the atoms. Energy dispersive X-ray (EDX) mapping of FeNi$_{AC}$-NC in Figure 1g also displayed the uniform distribution of Fe, Ni, and N elements on FeNi$_{AC}$-NC.
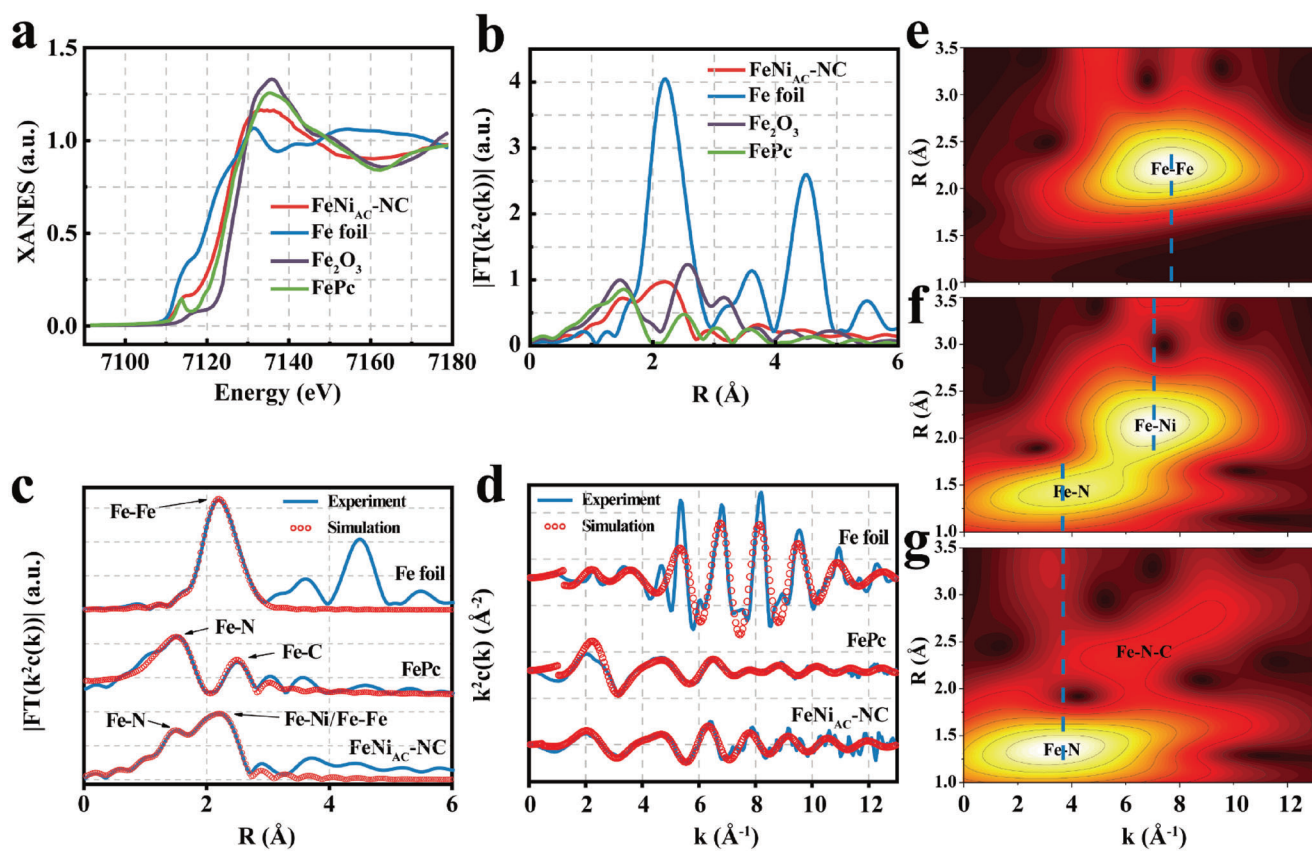
In order to investigate the coordination of the active central atoms (Fe, Ni, N) of the catalyst, X-ray absorption near-edge structure (XANES), extended X-ray absorption fine structure (EXAFS),

**ADVANCED
SCIENCE NEWS**

www.advancedsciencenews.com

**NANO · MICRO
small**
www.small-journal.com

Figure 1. a) Schematic diagram of the synthesis process of FeNi$_{AC}$-NC; b) XRD of catalysts with and without metal; c) TEM of FeNi$_{AC}$-NC; d) HAADF-STEM of FeNi$_{AC}$-NC, showing Fe-Ni clusters dominant in FeNi$_{AC}$-NC; f,e) the HAADF-STEM and corresponding EEL spectrum; g) corresponding element mapping images of Fe, Ni and N in FeNi$_{AC}$-NC.

and a wavelet transform (WT) were carried out. As in **Figure 2**a, the Fe in the sample is at a higher valence than the zero valence of the Fe foil, and similar to that of FePc. Furthermore, the Fourier-transformed (FT) k^3-weighted χ(k)-function of EXAFS spectra in r-space suggests that the majority of Fe species are Fe–N and Fe–Ni (Figure 2b). In the Fourier-transform EXAFS curves, FePc and FeNiAC-NC show a strong peak at 1.50 Å, which is attributed to the Fe–N bond.[36] More importantly, the peak at 2.18 Å is attributed to the Fe-Ni bond.[37] The WT-EXAFS analysis provides a more intuitive description of the backscattered atoms with radial distance and k-space resolution. The Fe foil shows the highest intensity at 7.8 Å^{-1} (Figure 2e), which reflects the Fe–Fe scattering path, while in Figure 2f, the Fe in FeNi$_{AC}$-NC exhibits the highest intensity at 7.2 Å^{-1}, reflecting the Fe-Ni bonding.[38] Moreover, in Figure S1e,f, Supporting Information, the wavelet transform

of Ni foil and sample FeNi$_{AC}$-NC are compared, and the highest intensity of Ni foil appears at 7.1 Å^{-1}, which is lower than the highest intensity of FeNi$_{AC}$-NC (7.7 Å^{-1}), corroborating Fe-Ni bond formation. This is due to the combined effect of the interaction of Fe and Ni in the cluster and the interaction of the single Fe and Ni atoms. The FeNi$_{AC}$-NC and FePc in Figure 2f,g exhibit the highest intensity at the same position of 3.7 Å^{-1}, confirming that the coordination of Fe with N is similar to FePc, in agreement with the XANES analysis. The refined coordination environment was investigated by a quantitative least-squares EXAFS fitting analysis (Figure 2c,d), a typical FeN$_4$ structure exists for the catalyst FeNi$_{AC}$-NC. Similarly, we tested the XANES, EXAFS, and WT spectra of Ni in FeNi$_{AC}$-NC and obtained results suggesting that Ni has a similar form to that of Fe (Figure S1, Supporting Information). According to the fit listed in Table S1, Supporting

**ADVANCED
SCIENCE NEWS**

www.advancedsciencenews.com

NANO · MICRO

small

www.small-journal.com

Figure 2. a) Fe K-edge XANES and b) Fourier-transform EXAFS spectra of FeNi$_{AC}$-NC and reference samples; c) Fe K-edge EXAFS analysis in R and k, d) spaces; wavelet transforms of Fe foil (e), FeNi$_{AC}$-NC (f), and FePc (g) for the k^2-weighted χ(k) K-edge EXAFS signals.

Information, the coordination number of N with both Fe and Ni is 4. In general, there is a strong interaction between Fe and Ni due to the presence of clusters, and both FeNi clusters and single atoms can be coordinated and stabilized by NC substrates.

The structures of Fe and Ni in our prepared material were simulated by DFT calculations. The simulation and optimization process are discussed in the SI. **Figure 3** shows that the FeNi$_{AC}$-NC material has two distinct types of bonds: shorter bonds between metal atoms and N/C which anchor the metal atoms on the surface, and longer metal-metal bonds: Fe–Fe, Ni–Ni, or Fe–Ni. The experimental Ni EXAFS of FeNi$_{AC}$-NC shows features that resemble Ni-N/C of a single atom Ni catalyst as well as Ni foil-like features at large distances. The experimental Fe EXAFS of FeNi$_{AC}$-NC also show similar features to Ni, but the long-range features do not strongly overlap with the Fe foil. Using this information, model structures were created containing single metal atoms and metal clusters in different bonding environments containing nitrogen and carbon. Previous reports have suggested a pyridinic and pyrrolic-like nitrogen environment in a single-atom catalyst, which was also adopted in our simulations.[43–45] Figure S2, Supporting Information, for Fe and Figure S3, Supporting Information, for Ni shows simulated EXAFS of all the model structures. From Figure S2, Supporting Information, for single atom Fe, the dominant feature agrees well with the experimental Fe/Ni EXAFS in FeNi$_{AC}$-NC, which appears to be a metal-N/C bond, but the absence of the other peaks suggests single atom Fe/Ni

cannot be the only structure. There are two double-atom FeNi model structures, labelled FeNi 1, and FeNi 2. The structure labeled FeNi 1 does not have the metal-N/C peak at the correct position, unlike the structure with label FeNi 2. The structure with label 2 also has the correct placement of the second peak ≈2 Å, which agrees with the experimental Fe/Ni EXAFS in FeNi$_{AC}$-NC. Nevertheless, these structures are missing peaks at larger distances, indicative of additional metal-metal bond features in the EXAFS. Finally, any model structure with more than two atoms, as shown in Figure S2c,d,e and S3,b,c,d, Supporting Information, cannot place the metal-N/C bond correctly and shows multiple features ≈2 Å, which suggests that larger clusters are not anchored into the nitrogen-containing carbon matrix. To obtain the closest agreement with the experiment, our calculations show that the experimental EXAFS of Fe or Ni in FeNi$_{AC}$-NC is a mixture of di-atomic FeNi clusters, Fe bulk, and Ni bulk, while maintaining a 1:1 ratio of metal, as shown in Figure 3c,d. Note here that bulk refers to our simulated bulk spectra and should correspond to alloy nanoclusters in the experimental sample with bulk metal coordination environments. The wavelet transforms shown in Figure 2f for the FeNi$_{AC}$-NC show a smaller Fe-metal bond than Fe foil, indicating that Fe is bonded to Ni. Therefore, while single-atom Fe and Ni are present in small amounts, we believe di-atomic FeNi dominates the FeNi$_{AC}$-NC structure with a small portion of bulk Fe and Ni-like features from metal/alloy nanoclusters, which together comprise the experimental EXAFS.
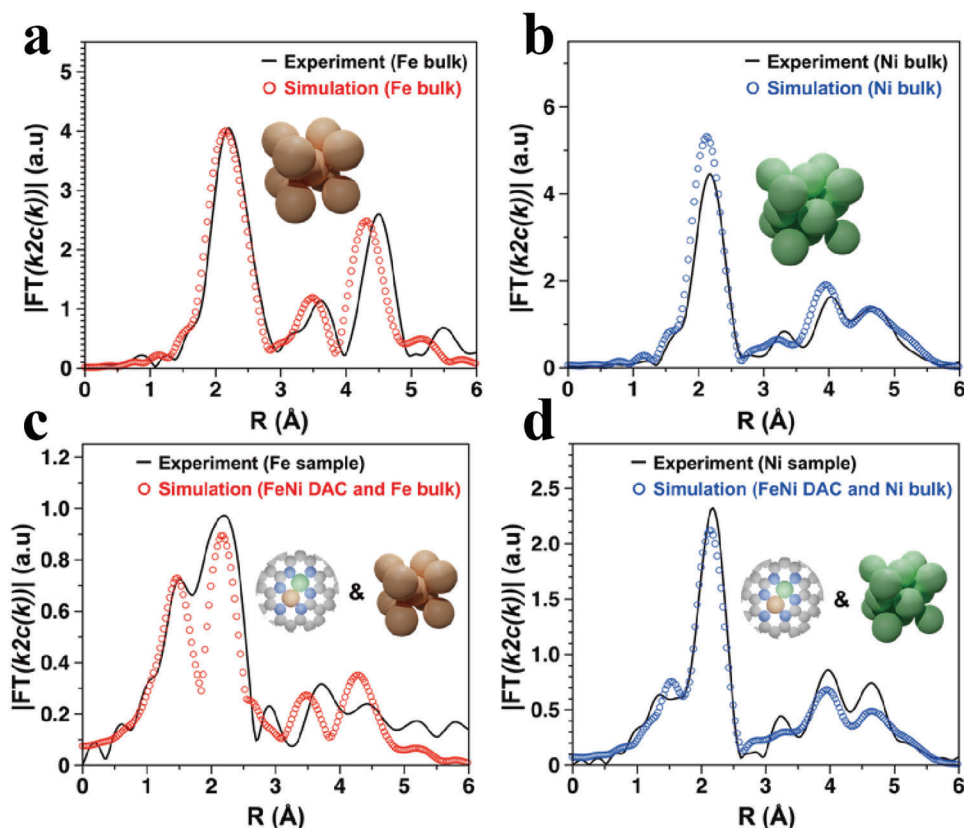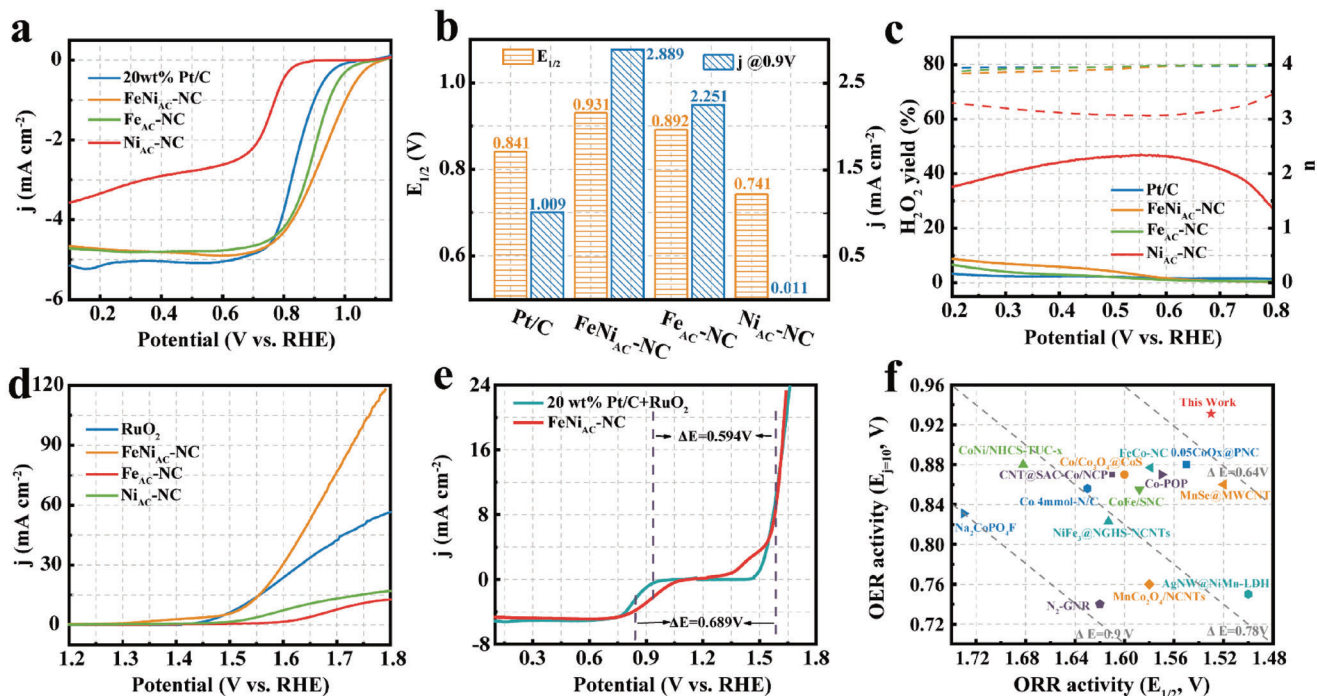
Figure 3. Comparison between the simulated and experimental EXAFS of a) Fe in Fe bulk, b) Ni in Ni bulk, c) Fe in predicted FeNi, and d) Ni in predicted FeNi after Fourier transforms at 300 K. Simulations for bulk Fe were performed using the BCC phase and bulk Ni using the FCC phase. Color scheme: brown (Fe) and green (Ni).

2.2. Half-Cell Tests and Analysis of Active Sites

The ORR electrocatalytic behaviors of the as-prepared catalysts were first evaluated by LSV measurements in 0.1 M KOH solution. FeNi$_{AC}$-NC had the most positive half-wave potential ($E_{1/2}$) of 0.936 V, which is significantly higher than that of Fe$_{AC}$-NC ($E_{1/2}$ = 0.892 V), Ni$_{AC}$-NC($E_{1/2}$ = 0.741 V) and commercial 20 wt.% Pt/C ($E_{1/2}$ = 0.841 V) (**Figure** 4a). The oxygen reduction process of the different samples is then discussed. Both from the results of rotating ring disc electrode measurements (Figure 4c) and the LSV curves at different revolutions fitted by the K–L equation (Figure S4b, Supporting Information), FeNi$_{AC}$-NC show a four-electron transfer, which avoids the production of H_2O_2 by a two-electron process, while the two-electron processes occurred on Ni$_{AC}$-NC. In addition, FeNi$_{AC}$-NC also showed excellent stability, maintaining 92% of the current at a constant potential of 0.8 V for 25 h (Figure S4d, Supporting Information) and good methanol tolerance compared to Pt/C (Figure S4c, Supporting Information), and no any significant change was found in XRD and TEM (Figure S5, Supporting Information) of the sample that after long-time ORR test, which also confirms its good stability. Further, the roles played by Fe and Ni of FeNi$_{AC}$-NC in the electrocatalytic process were explored in detail; the corresponding experiments are described in the SI. As shown in Table S2, Supporting Information, the excellent anchoring ability of phenanthroline and our unique synthesis method provides an opportunity

to prepare catalysts with different Fe/Ni ratios. The XRD results in Figure S6a, Supporting Information, suggest that with the addition of nickelocene, Ni can enter the lattice of Fe, bond with Fe, make the lattice of Fe expand, and form an alloy. The ORR results of the samples with various Fe/Ni ratios are shown in Figure S6b, Supporting Information. Although the ORR activity of Ni$_{AC}$-NC is far lower than that of Fe$_{AC}$-NC, the introduction of an appropriate quantity of Ni can significantly improve the performance of the FeNi-NC catalyst because Ni affects the stability of ORR reaction intermediates when coupled with Fe. When the Ni doping amount is more than Fe, the ORR performance of the catalyst is reduced. Thus, more Fe content does not guarantee better performance because the best activity for ORR was found for the sample with a Fe to Ni ratio of 1:1 which means both Fe and Ni contribute towards ORR activity, as explained in Section 2.4. The samples with different total metal contents were optimized as shown in Figure S7, Supporting Information.

Understanding the interactions between different sites has long been a challenge for multi-active-site catalysts, which is limited by the precise control of the catalyst synthesis. Furthermore, the increased activity from the synergistic interaction of multiple sites must be distinguished from other factors, such as the number of active sites. Here, benefiting from the limited anchoring effect of phenanthroline on the metal, our proposed method provides a possibility to discuss the interaction of Fe, Ni di-atomics and clusters, and diatomic catalysts-R-FeNi$_{DA}$-NC with high Fe

**ADVANCED
SCIENCE NEWS**

www.advancedsciencenews.com

**NANO · MICRO
small**

www.small-journal.com

Figure 4. Evaluation of electrocatalytic performance of FeNi$_{AC}$-NC for ORR and OER. a) LSV curves of different samples for ORR in O$_2$-saturated 0.1 M KOH solution with 5 mV s^{-1} at a rotation rate 1600 rpm; b) comparison of E$_{1/2}$ and $^{JK@0.9 V}$ of different catalysts; c) electron transfer number (right) and H$_2$O$_2$ yield (left) versus potential; d) LSV curves of Fe$_{AC}$-NC, Ni$_{AC}$-NC, FeNi$_{AC}$-NC and Pt/C for OER in 1 M KOH solution with a sweep rate 5 mV s^{-1}; e) overall polarization curves of, FeNi$_{AC}$-NC and Pt/C+RuO$_2$ for bifunctional catalytic activity tests; f) comparison of ΔE (Δ$E = E_{j10} - E_{1/2}$) between FeNi$_{AC}$-NC catalysts and other catalysts reported in recent years (Table S3, Supporting Information)

content (Fe wt.% = 0.811%), and atom-cluster catalysts-R-FeNi$_{AC}$-NC with a low Fe content (Fe wt.% = 0.713%) were prepared (Figure S8a). Since a portion of the Fe in the clusters are not fully used as adsorption sites, it was possible to obtain fewer Fe active sites for R-FeNi$_{AC}$-NC than for R-FeNi$_{DA}$-NC. Under these conditions, R-FeNi$_{AC}$-NC exhibited comparable catalytic activity to that of R-FeNi$_{AC}$-NC (Figure S8b, Supporting Information), which suggests that the interaction between FeNi clusters and Fe/Ni diatoms promotes its ORR performance. DFT calculations were performed to address the difference between the electrochemical activity of R-FeNi$_{AC}$-NC, and R-FeNi$_{DA}$-NC synthesized in our work, as shown in Figures 6c and d, Supporting Information. The smaller overpotential for ORR in the presence of a small cluster is consistent with the experimental observation in Figure S8b, but we note that this is a relatively small difference is within our computational uncertainty.

Zinc-air batteries have a high requirement for OER performance at the air electrode. FeNi$_{AC}$-NC performs well for OER (Figure 4d), delivering the same overpotential at 10 mA cm^{-2} as commercial RuO$_2$ (300 mV); this is also significantly lower than Fe$_{AC}$-NC (504 mV) and Ni$_{AC}$-NC (410 mV), which is consistent with previous reports that Fe and Ni synergy can effectively catalyze the OER. Moreover, at a high current density of 50 mA cm^{-2}, FeNi$_{AC}$-NC (414 mV) has a lower overpotential than commercial RuO$_2$ (514 mV) which could be due to a higher electrochemical active surface area of FeNi$_{AC}$-NC (11.67 mF cm^{-2}) as compared to RuO$_2$ (4.07 mF cm^{-2}) (Figure S8c, Supporting Information). This observation indicates that FeNi$_{AC}$-NC has more

evenly distributed active sites for adsorption and catalytic reactants resulting in significantly higher utilization of active sites due to its unique configuration compared to RuO$_2$, even at high current density. In bifunctional catalysts, ΔE ($E_{@10-} E_{1/2}$) is an important indicator of performance. As shown in Figure 4e, the ΔE of FeNi$_{AC}$-NC is 0.594 V, which is smaller than Pt/C-RuO$_2$ (ΔE = 0.689 V). In addition, the ΔE of 0.594 V is competitive with the recently reported state-of-the-art bifunctional catalysts (Figure 4f) that provide good conditions for the assembly of zinc-air batteries.

2.3. Exploration of Preparation Methods

To examine the feasibility of our proposed one-step pyrolysis approach, a more detailed observation was carried out. As shown in **Figure 5**a, since phenanthroline has a low melting temperature (117 °C) and ferrocene/nickelocene has a low vaporization temperature (100 °C), they are easily adsorbed on AC and into the pores of AC during the heating process. Further, since phenanthroline has a tricyclic conjugate plane, which can enhance the electron cloud density of the N atom on the aromatic ring and facilitate the transfer of electrons between atoms, it is easy to coordinate with metals and form metal-N structures on the surface of AC.[46] The coordination ability of phenanthroline to ferrocene at 200 °C was confirmed by NMR (Figure 5b). A careful investigation of the XPS, in addition to the pyridine-N peak which is consistent with phenanthroline, the N1s spectrum shows an
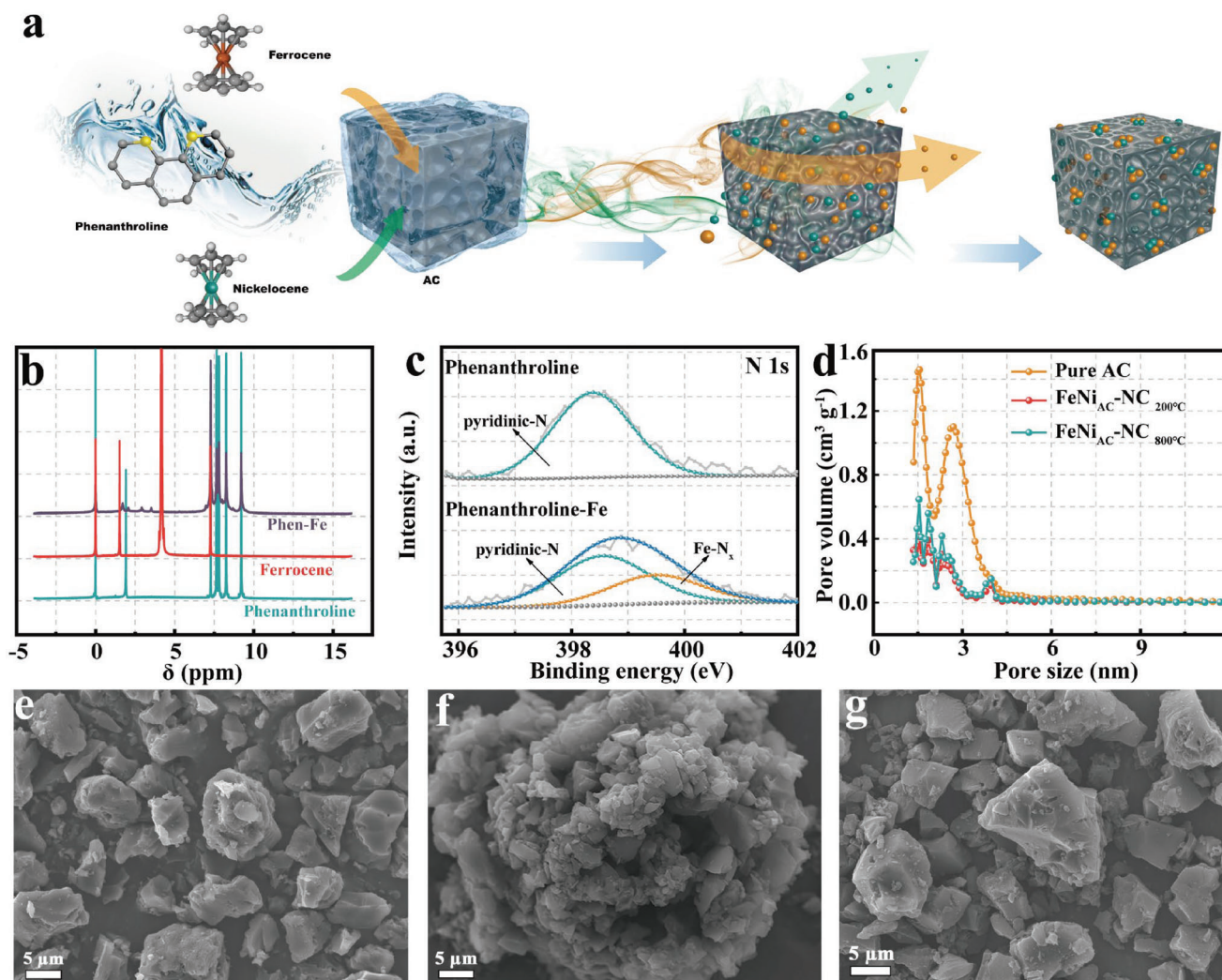
Figure 5. a) Schematic diagram of the synthesis process; b) NMR hydrogen spectra of ferrocene, a mixture of ferrocene with phenanthroline, and the products after annealing at 200 °C for phenanthroline alone; c) deconvoluted N1s XPS spectra of 200 °C annealing phenanthroline and 200 °C annealing phenanthroline-Fe; d) pore size distribution of different samples; e-g) FESEM of pure AC, $FeNi_{AC}$-$NC_{200\,°C}$ and $FeNi_{AC}$-$NC_{800\,°C}$.

Fe–N_x peak at 399.5 eV consistent with FePc[39] (Figure 5c), which indicates that the structure of the target catalysts can be precisely tuned by the coordination between phenanthroline and metal sources in the pre-synthesis stage of the material.

There is no doubt that M-N can be formed on the outer surface of AC, but the relevant question is if it can be formed on the inner pores wall of AC? The BET data shown in Figure 5d answers this question. From the pore size versus pore volume distribution of the samples displayed in Figure 5d, it is clear that the pore volume of $FeNi_{AC}$-$NC_{200\,°C}$ decreases significantly as compared to that of pure activated carbon (from 1.125 cm³ g⁻¹ to 0.382 cm³ g⁻¹), which indicates that the liquid phenanthroline and gasified ferrocene/nickelocene are adsorbed on and into the pores of AC at 200 °C. With further annealing to 800 °C, the pore volume of the sample increases to 0.571 cm³ g⁻¹, which suggests that the phenanthroline carbonizes and reopens some of the pores (Figure 5d). SEM observations support this point (Figure 5e–g and S10, Supporting Information): judging from

the low magnification FESEM, the $FeNi_{AC}$-$NC_{200\,°C}$ are bound together, and from the high magnification FESEM, the surface of $FeNi_{AC}$-$NC_{200\,°C}$ is covered by a rough wrinkled film. After further annealing to 800 °C, the phenanthroline is carbonized, and the surface of $FeNi_{AC}$-NC_{800} becomes smooth and similar to AC.

In order to understand the anchoring capacity of phenanthroline to the metal, more samples were prepared by adding different amounts of metal with the phenanthroline fixed. The XRD (Figure S11a, Supporting Information) shows an increased metal peak with increasing metal feeding, indicating the formation of larger nanoparticles at high content, which was confirmed by the TEM images (Figure S11b,c).

In addition, we extended this method to prepare FeCo catalysts and found that $FeCo_{AC}$-NC has the same excellent ORR performance, highly selective 4-electron transfer, and good methanol tolerance (Figure S12, Supporting Information). However, the $CoNi_{AC}$-NC activity is poor (Figure S13, Supporting
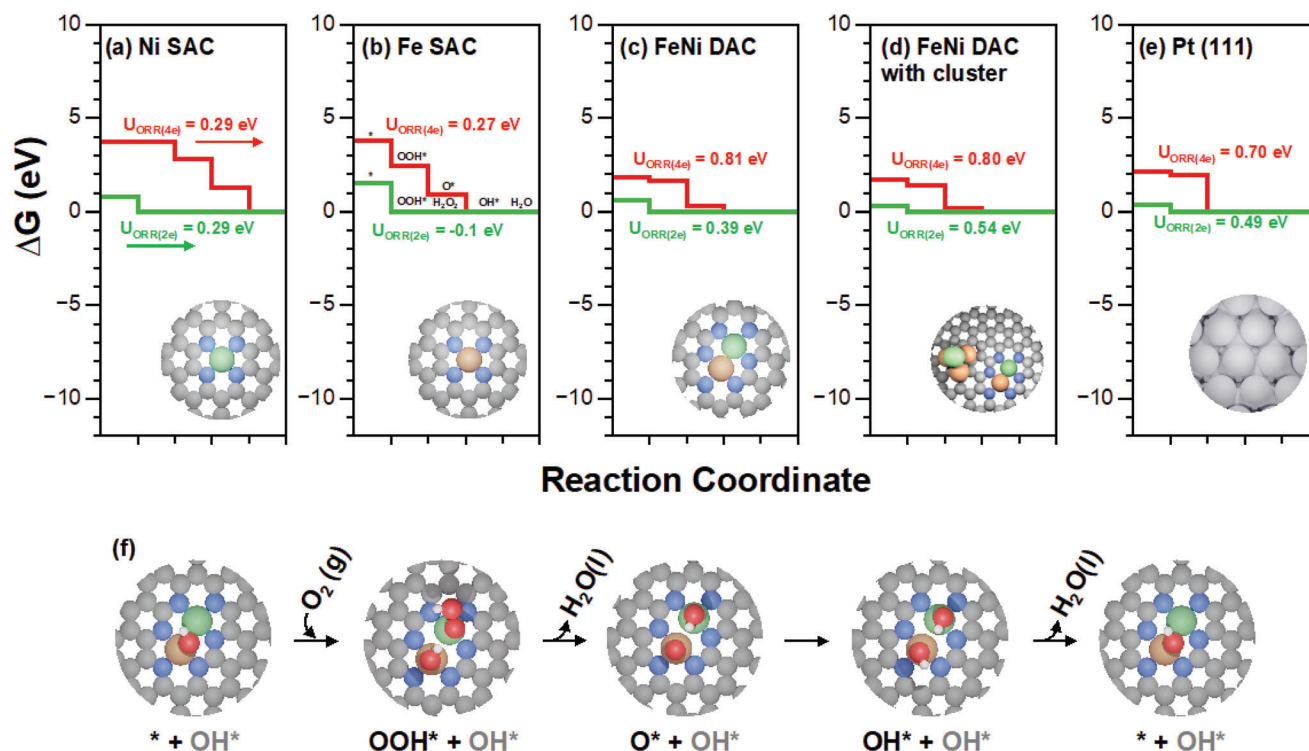
Figure 6. Gibbs free energy diagram for ORR on a) Ni SAC, b) Fe SAC, c) FeNi DAC, d) Fe Ni DAC with cluster, and e) Pt (111) surface and ORR reaction mechanism on FeNi DAC is shown in (f). Color scheme: blue (nitrogen), orange (iron), green (nickel), red (oxygen), white (hydrogen), dark grey (carbon).

Information), which indicates that for such FeM-NC catalysts, the active site of ORR originates from Fe as the center, while Ni and Co act as modulators. The successful synthesis of FeCo and CoNi allows this method to be widely used for the preparation of M1M2-NC.
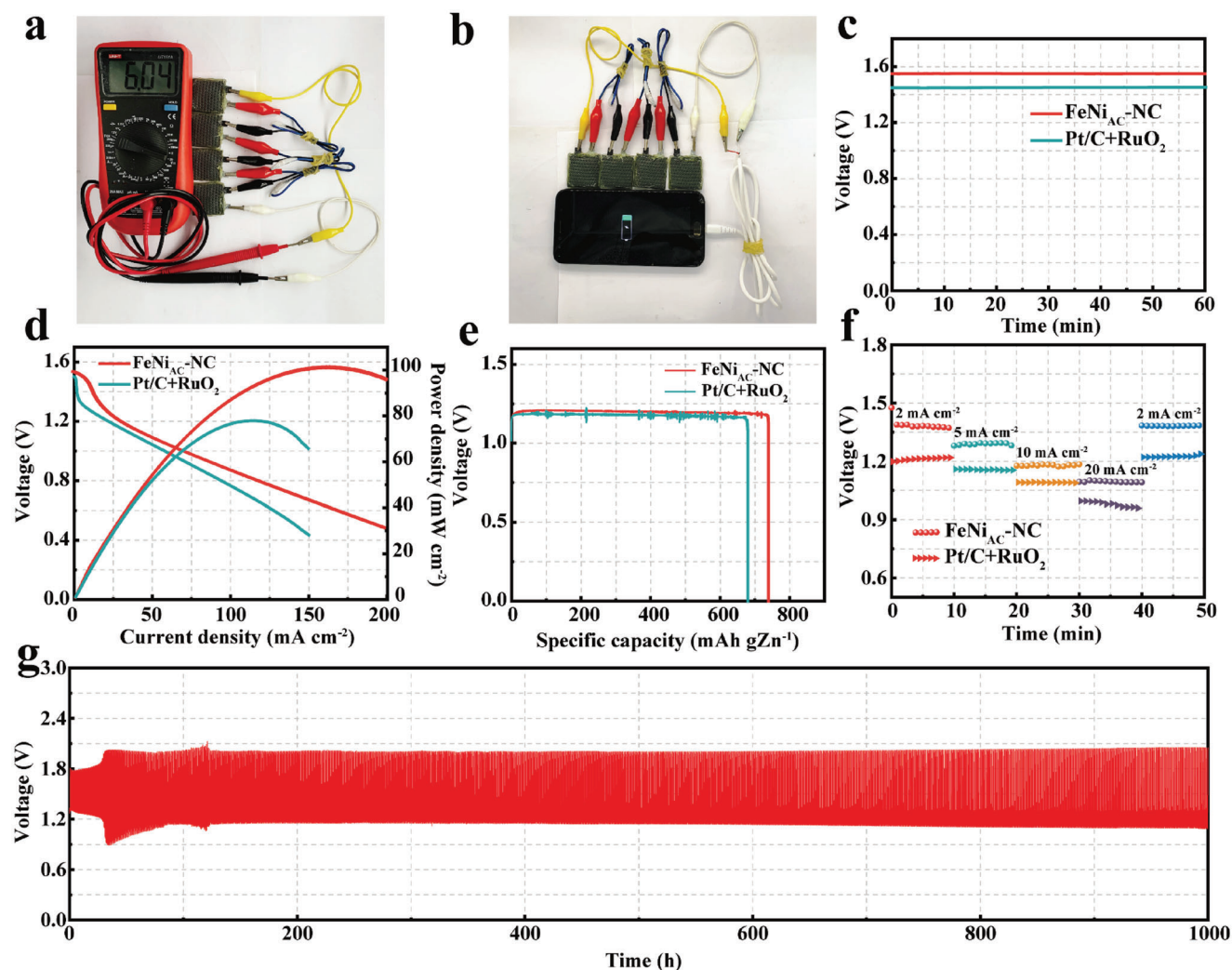
2.4. The Excellent Performance of FeNiAC-NC was Investigated from DFT Calculations

DFT calculations were performed to compare the electrochemical performance of our predicted FeNi$_{AC}$-NC structure with single atom Fe, single atom Ni, and a Pt (111) surface. To evaluate the ORR activity, the binding energies of the reaction intermediates were calculated using the methodology described in the SI. Although our EXAFS calculation suggests the presence of bulk like Fe and Ni features combined with di-atomic FeNi, the activity of the FeNi$_{AC}$-NC system is dominated by di-atomic FeNi, and we chose that as our model system, as shown in **Figure 6**c. For FeNi$_{AC}$-NC, our calculation suggests that the Fe site is pre-covered with –OH in the aqueous environment. The binding energies of the intermediate species are tabulated in **Table 1**. For single atom Fe catalyst, the strong binding of the –OH* intermediate makes Step 4 the rate-determining step (RDS) with a high overpotential of 0.96 V as shown in Figure 6b, which is consistent with previous reports in the literature[35]. For single-atom Ni catalysts, the two-electron process is reported to be dominant over the four-electron process, as shown in Figure 4c. The calculated overpotential for both processes is 0.93 V as shown in

Figure 6a, which is due to the weak binding of OOH* in the four-electron process, resulting in limited H$_2$O formation, making Step 1 the RDS. For Pt, the binding energy of O* is too weak, and OH* binding is too strong, which limits the ORR activity with an overpotential of 0.52 V as shown in Figure 6e, in agreement with the literature. For FeNi$_{AC}$-NC, Fe and Ni sites exist together and calculations demonstrate a synergistic effect between the metals. As mentioned before, Fe sites are pre-covered with -OH* sites due to strong binding in the aqueous environment. Hence, the ORR proceeds on the Ni site where –OOH* binding is now stronger than single atom Ni. Hence –OOH* step is no longer the RDS for ORR reaction making this material better than single atom Ni. After Step 1, H$_2$O formation in Step 2 leads to the formation of –OH on Ni and –O on the Fe sites. The binding energy of –O on the Fe site is weaker than on single atom Fe. This weaker binding enables the formation of –OH in Step 4, which is bound weakly on the Fe site in the presence of –OH on Ni. The weaker binding of –OH in Step 4 leads to a smaller

Table 1. Binding energy of reaction intermediates for different model systems to calculate Gibbs free energy for ORR (eV).

	Ni SAC	Fe SAC	Pt (111)	FeNi-DAC	FeNi-DAC-with cluster
-O*	3.59	1.47	1.42	2.21	1.82
-OH*	1.53	0.28	1.06	0.91	0.80
-OOH*	4.35	3.27	4.09	3.87	3.82

**ADVANCED
SCIENCE NEWS**

www.advancedsciencenews.com

NANO · MICRO

small

www.small-journal.com

Figure 7. a) Voltage test of four in-house pouch Zn-air batteries; b) the four Zn-air pouch batteries are continuously charged for a 5 V input smartphone; c) open circuit voltage curves of the FeNi$_{AC}$-NC and Pt/C+RuO$_2$; d) the discharge polarization curves and power density curves of the battery using the FeNi$_{AC}$-NC and Pt/C+RuO$_2$ air electrodes; e) long-term galvanostatic discharge curves of Zn-air batteries before complete consumption of the Zn anode at 10 mA cm^{-2}, the specific capacity was normalized to the mass of consumed Zn; f) discharge curve at different current densities of FeNi$_{AC}$-NC and Pt/C+RuO$_2$; g) long-time galvanostatic cycling test at 2.0 mA cm^{-2}.

overpotential of 0.43 V as shown in Figure 6c. Hence, the synergistic effect of both metals makes FeNi$_{AC}$-NC suitable for ORR with a smaller overpotential, which agrees with the experimental observations.

2.5. Assembly of Full Cells

Prior to this, significant work was done to move zinc-air batteries toward flexibility.[40–42] Due to its flexible shape, light weight, and good stability, pouch batteries are widely used. To evaluate the performance of this catalyst in practical applications, in-house pouch Zn-air batteries (PZABs) were assembled with a 6 M KOH, 0.2 M zinc acetate solution, and PZABs were also assembled by using Pt/C+RuO$_2$ under same conditions, for comparison. As shown in Figure 7a, four PZABs exhibiting high output voltage are able to charge a smartphone continuously. A FeNi$_{AC}$-NC-

based PZAB delivers an open circuit voltage of 1.55 V, which is higher than that of Pt/C+RuO$_2$-based PZAB (1.45 V), and also exhibits excellent stability. Figure 7b further shows that the peak power density of a FeNi$_{AC}$-NC-based PZAB can reach 101.4 mW cm^{-2}, far higher than that of noble metal catalysts (Pt/C+RuO$_2$) based PAZB (77.9 mW cm^{-2}). In a practical discharge situation, as shown in Figure 7d,e, at 10 mA cm^{-2}, the PZAB assembled by FeNi$_{AC}$-NC shows a higher specific capacity of 739.3 mA h g^{-1} (normalized to the weight of the consumed zinc electrode) than that of the PZAB assembled with the noble metal (680.2 mA h g^{-1}). Moreover, the PZAB based on FeNi$_{AC}$-NC shows good stability and high discharge voltage at different current densities (Figure 7f). More exciting, in long charge and discharge cycles at 2 mA cm^{-2}, the FeNi$_{AC}$-NC-based PZAB exhibited excellent stability over 1000 h, 500 cycles. This demonstrates the great potential of FeNi$_{AC}$-NC as a cathode material for zinc-air batteries. This is also sufficient to prove the stability of the catalyst and our

ADVANCED
SCIENCE NEWS

www.advancedsciencenews.com

NANO · MICRO
small

www.small-journal.com

self-assembled pouch Zn-air batteries. It opens up the possibility of wider application of zinc-air batteries.

3. Conclusion

In conclusion, we propose a facile one-step pyrolysis method for the preparation of FeNi$_{AC}$-NC bimetallic cluster catalysts, and further successfully prepared sub-nanometer bimetallic clusters (FeCo and CoNi) without using any solvent. Experiments and theoretical calculations show that the FeNi$_{AC}$-NC bimetallic cluster catalyst shows an excellent ORR activity of $E_{1/2} = 0.936$ V; much higher than that of commercial Pt/C ($E_{1/2} = 0.841$ V), due to the synergistic effect of uniformly dispersed Fe/Ni di-atomic clusters and larger Fe/Ni nanoclusters on N-doped carbon substrate. In addition, FeNi$_{AC}$-NC also shows superior OER performance to commercial RuO$_2$, which makes it a great candidate for rechargeable zinc-air batteries. In-house pouch Zn-air batteries assembled by FeNi$_{AC}$-NC exhibits stability over 500 cycles and 1000 h. These findings provide an important reference for the atomic structure tuning, large-scale preparation, and commercial application of nanocluster catalysts in Zn–Air cells.

Supporting Information

Supporting Information is available from the Wiley Online Library or from the author.

Conflict of Interest

The authors declare no conflict of interest.

Data Availability Statement

The data that support the findings of this study are available in the supplementary material of this article.

Keywords

in-house pouch Zn-air battery, one-step synthesis, sub-nanocatalyst, solvent-free, synergistic effect

[1] Y. Tan, W. Zhu, Z. Zhang, W. Wu, R. Chen, S. Mu, H. Lv, N. Cheng, *Nano Energy* **2021**, *83*, 105813.
[2] Y. Jiang, Y.-P. Deng, R. Liang, N. Chen, G. King, A. Yu, Z. Chen, *J. Am. Chem. Soc.* **2022**, *144*, 4783.
[3] Y. Zhu, K. Yue, C. Xia, S. Zaman, H. Yang, X. Wang, Y. Yan, B. Y. Xia, *Nanomicro Lett.* **2021**, *13*, 137.
[4] C. X. Zhao, J. N. Liu, J. Wang, D. Ren, J. Yu, X. Chen, B. Q. Li, Q. Zhang, *Adv. Mater.* **2021**, *33*, 2008606.
[5] Y. Yan, S. Liang, X. Wang, M. Zhang, S. M. Hao, X. Cui, Z. Li, Z. Lin, *Proc. Natl. Acad. Sci. U. S. A.* **2021**, *118*, 2110036118.
[6] H. Xu, D. Wang, P. Yang, L. Du, X. Lu, R. Li, L. Liu, J. Zhang, M. An, *Appl. Catal. B* **2022**, *305*, 121040.
[7] J. Song, Y. Chen, H. Huang, J. Wang, S. C. Huang, Y. F. Liao, A. E. Fetohi, F. Hu, H. Y. Chen, L. Li, X. Han, K. M. El-Khatib, S. Peng, *Adv. Sci.* **2022**, *9*, 2104522.
[8] H. Huang, A. Huang, D. Liu, W. Han, C. H. Kuo, H. Y. Chen, L. Li, H. Pan, S. Peng, *Adv. Mater.* **2023**, *35*, 2303109.
[9] J. Song, S. Qiu, F. Hu, Y. Ding, S. Han, L. Li, H.-Y. Chen, X. Han, C. Sun, S. Peng, *Adv. Funct. Mater.* **2021**, *31*, 2100618.
[10] D. Yu, Y. Ma, F. Hu, C.-C. Lin, L. Li, H.-Y. Chen, X. Han, S. Peng, *Adv. Energy Mater.* **2021**, *11*, 2101242.
[11] C.-X. Zhao, B.-Q. Li, J.-N. Liu, Q. Zhang, *Angew. Chem., Int. Ed.* **2021**, *60*, 4448.
[12] X. Su, S. Hao, T. P. Bailey, S. Wang, I. Hadar, G. Tan, T.-B. Song, Q. Zhang, C. Uher, C. Wolverton, X. Tang, M. G. Kanatzidis, *Adv. Energy Mater.* **2018**, *8*, 1800659.
[13] T. Yan, N. Li, L. Wang, Q. Liu, F. M. Ali, L. Wang, Y. Xu, Y. Liang, Y. Dai, B. Huang, J. You, G. A. Ozin, *Energy Environ. Sci.* **2020**, *13*, 3054.
[14] Z. Li, Z. Zhuang, F. Lv, H. Zhu, L. Zhou, M. Luo, J. Zhu, Z. Lang, S. Feng, W. Chen, L. Mai, S. Guo, *Adv. Mater.* **2018**, *30*, 1803220.
[15] J. Wei, D. Xia, Y. Wei, X. Zhu, J. Li, L. Gan, *ACS Catal.* **2022**, *12*, 7811.
[16] M. Xiao, Z. Xing, Z. Jin, C. Liu, J. Ge, J. Zhu, Y. Wang, X. Zhao, Z. Chen, *Adv. Mater.* **2020**, *32*, 2004900.
[17] W. Zhang, Y. Chao, W. Zhang, J. Zhou, F. Lv, K. Wang, F. Lin, H. Luo, J. Li, M. Tong, E. Wang, S. Guo, *Adv. Mater.* **2021**, *33*, 2102576.
[18] Z. Chen, X. Su, J. Ding, N. Yang, W. Zuo, Q. He, Z. Wei, Q. Zhang, J. Huang, Y. Zhai, *Appl. Catal. B* **2022**, *308*, 121206.
[19] J. Wang, W. Liu, G. Luo, Z. Li, C. Zhao, H. Zhang, M. Zhu, Q. Xu, X. Wang, C. Zhao, Y. Qu, Z. Yang, T. Yao, Y. Li, Y. Lin, Y. Wu, Y. Li, *Energy Environ. Sci.* **2018**, *11*, 3375.
[20] C. Y. Su, H. Cheng, W. Li, Z. Q. Liu, N. Li, Z. Hou, F. Q. Bai, H. X. Zhang, T. Y. Ma, *Adv. Energy Mater.* **2017**, *7*, 1602420.
[21] H. Li, J. Wang, R. Qi, Y. Hu, J. Zhang, H. Zhao, J. Zhang, Y. Zhao, *Appl. Catal. B* **2021**, *285*, 119778.
[22] J. Lilloja, E. Kibena-Põldsepp, A. Sarapuu, M. Käärik, J. Kozlova, P. Paiste, A. Kikas, A. Treshchalov, J. Leis, A. Tamm, V. Kisand, S. Holdcroft, K. Tammeveski, *Appl. Catal. B* **2022**, *306*, 121113.
[23] H. Huang, D. Yu, F. Hu, S. C. Huang, J. Song, H. Y. Chen, L. L. Li, S. Peng, *Angew. Chem., Int. Ed.* **2022**, *61*, 202116068.
[24] M. Liu, J. Lee, T.-C. Yang, F. Zheng, J. Zhao, C.-M. Yang, L. Y. S. Lee, *Small Methods* **2021**, *5*, 2001165.
[25] X. Wan, Q. Liu, J. Liu, S. Liu, X. Liu, L. Zheng, J. Shang, R. Yu, J. Shui, *Nat. Commun.* **2022**, *13*, 2963.
[26] Y. Wang, Q. Li, L.-C. Zhang, Y. Wu, H. Chen, T. Li, M. Xu, S.-J. Bao, *J. Mater. Chem. A* **2021**, *9*, 7137.
[27] Y. Chen, J. Lin, B. Jia, X. Wang, S. Jiang, T. Ma, *Adv. Mater.* **2022**, 2201796.
[28] J. Wang, Z. Li, Y. Wu, Y. Li, *Adv. Mater.* **2018**, *30*, 1801649.
[29] L. Zhang, Q. Wang, L. Li, M. N. Banis, J. Li, K. Adair, Y. Sun, R. Li, Z.-J. Zhao, M. Gu, X. Sun, *Nano Energy* **2022**, *93*, 106813.
[30] J. Guo, X. Yan, Q. Liu, Q. Li, X. Xu, L. Kang, Z. Cao, G. Chai, J. Chen, Y. Wang, J. Yao, *Nano Energy* **2018**, *46*, 347.
[31] Y. Wang, F.-L. Hu, Y. Mi, C. Yan, S. Zhao, *Chem. Eng. J.* **2021**, *406*, 127135.

**ADVANCED
SCIENCE NEWS**

www.advancedsciencenews.com

NANO · MICRO

small

www.small-journal.com

[32] Z. Li, D. Wang, Y. Wu, Y. Li, *Natl. Sci. Rev.* **2018**, *5*, 673.

[33] J. Liu, *ACS Catal.* **2016**, *7*, 34.

[34] X. Zhang, S. Zhang, Y. Yang, L. Wang, Z. Mu, H. Zhu, X. Zhu, H. Xing, H. Xia, B. Huang, J. Li, S. Guo, E. Wang, *Adv. Mater.* **2020**, *32*, 1906905.

[35] J.-C. Liu, H. Xiao, J. Li, *J. Am. Chem. Soc.* **2020**, *142*, 3375.

[36] X. Wang, Y. Jia, X. Mao, D. Liu, W. He, J. Li, J. Liu, X. Yan, J. Chen, L. Song, A. Du, X. Yao, *Adv. Mater.* **2020**, *32*, 2000966.

[37] F. Dong, M. Wu, Z. Chen, X. Liu, G. Zhang, J. Qiao, S. Sun, *Nano-Micro Lett.* **2022**, *14*, 36.

[38] D. Yu, Y. Ma, F. Hu, C. C. Lin, L. Li, H. Y. Chen, X. Han, S. Peng, *Adv. Energy Mater.* **2021**, *11*, 2101242.

[39] K. Liu, J. Fu, Y. Lin, T. Luo, G. Ni, H. Li, Z. Lin, M. Liu, *Nat. Commun.* **2022**, *13*, 2075.

[40] M. D. Hossain, Y. Huang, T. H. Yu, W. A. Goddard Iii, Z. Luo, *Nat. Commun.* **2020**, *11*, 2256.

[41] S. A. Abbas, J. T. Song, Y. C. Tan, K. M. Nam, J. Oh, K.-D. Jung, *ACS Appl. Energy Mater.* **2020**, *3*, 8739.

[42] P. G. Sammes, G. Yahioglu, *Chem. Soc. Rev.* **1994**, *23*, 327.

[43] H. Yang, L. Shang, Q. Zhang, R. Shi, G. I. N. Waterhouse, L. Gu, T. Zhang, *Nat. Commun.* **2019**, *10*, 4585.

[44] Z. Pei, Z. Yuan, C. Wang, S. Zhao, J. Fei, L. Wei, J. Chen, C. Wang, R. Qi, Z. Liu, Y. Chen, *Angew. Chem., Int. Ed.* **2020**, *59*, 4793.

[45] F. Qiang, J. Feng, H. Wang, J. Yu, J. Shi, M. Huang, Z. Shi, S. Liu, P. Li, L. Dong, *ACS Catal.* **2022**, *12*, 4002.

[46] Y. Zhang, Y.-P. Deng, J. Wang, Y. Jiang, G. Cui, L. Shui, A. Yu, X. Wang, Z. Chen, *Energy Storage Mater.* **2021**, *35*, 538.